Analytical and Bioanalytical Chemistry (2024) 416:1745–1757
https://doi.org/10.1007/s00216-024-05178-z

RESEARCH PAPER

Spatial MS multiomics on clinical prostate cancer tissues

Jacob X. M. Truong[1,2,3,4] · Sushma R. Rao[1,2] · Feargal J. Ryan[2,5] · David J. Lynn[2,5] · Marten F. Snel[1,2] · Lisa M. Butler[1,2,3,4] · Paul J. Trim[1,2]

Received: 7 December 2023 / Revised: 19 January 2024 / Accepted: 22 January 2024 / Published online: 7 February 2024

Abstract

Mass spectrometry (MS) and MS imaging (MSI) are used extensively for both the spatial and bulk characterization of samples in lipidomics and proteomics workflows. These datasets are typically generated independently due to different requirements for sample preparation. However, modern omics technologies now provide higher sample throughput and deeper molecular coverage, which, in combination with more sophisticated bioinformatic and statistical pipelines, make generating multiomics data from a single sample a reality. In this workflow, we use spatial lipidomics data generated by matrix-assisted laser desorption/ionization MSI (MALDI-MSI) on prostate cancer (PCa) radical prostatectomy cores to guide the definition of tumor and benign tissue regions for laser capture microdissection (LCM) and bottom-up proteomics all on the same sample and using the same mass spectrometer. Accurate region of interest (ROI) mapping was facilitated by the SCiLS region mapper software and dissected regions were analyzed using a dia-PASEF workflow. A total of 5525 unique protein groups were identified from all dissected regions. Lysophosphatidylcholine acyltransferase 1 (LPCAT1), a lipid remodelling enzyme, was significantly enriched in the dissected regions of cancerous epithelium (CE) compared to benign epithelium (BE). The increased abundance of this protein was reflected in the lipidomics data with an increased ion intensity ratio for pairs of phosphatidylcholines (PC) and lysophosphatidylcholines (LPC) in CE compared to BE.

Keywords Multiomics · MALDI imaging · Lipidomics · Proteomics · Laser capture microdissection · Prostate cancer

Introduction

Multiomics refers to the analysis and integration of multiple ‘omics data sets from the same sample. For many years, mass spectrometry (MS) has been a key technology used in omics research, particularly for proteomics [1] and lipidomics [2]. The bulk analysis used in most MS ‘omics experiments typically involves sample homogenization, isolation or enrichment of the analyte class of interest, and chromatographic separation, e.g., liquid chromatography (LC), followed by mass analysis. A considerable limitation associated with bulk analysis of tissues is the need for sample homogenization which results in an average measurement of each analyte across a mixture of cell types. This limitation is particularly problematic for heterogeneous tissues such as prostate cancer (PCa) and breast cancer samples where tumors are often multi-focal and there is significant inter and intra-patient heterogeneity [3]. MS imaging (MSI) addresses this limitation by acquiring data in situ from thin tissue sections. In MSI, individual mass spectra are acquired at discrete *x*–*y* locations enabling the visualization of the relative

✉ Paul J. Trim
Paul.Trim@sahmri.com

1 The University of Adelaide, North Terrace, Adelaide, SA 5000, Australia

2 South Australian Health and Medical Research Institute (SAHMRI), North Terrace, Adelaide, South Australia 5000, Australia

3 Freemasons Centre for Male Health and Wellbeing, University of Adelaide, North Terrace, Adelaide, South Australia 5000, Australia

4 South Australian immunoGENomics Cancer Institute (SAiGENCI), North Terrace, Adelaide, South Australia 5000, Australia

5 Flinders Health and Medical Research Institute, Flinders University, Bedford Park, South Australia 5042, Australia

abundance and spatial localization of analytes. This spatially resolved technology has proven utility for the analysis of small molecular weight analytes, such as lipids [4], metabolites, and small molecule drugs [5]. In situ 'omics analyses of different analyte classes (e.g., proteins and lipids) using MSI are usually performed independently and on separate samples. This is mainly a consequence of the specific sample preparation requirements to extract and enrich each of these analytes. For instance, peptides are often prepared for MSI on fresh-frozen tissue by first washing with a high organic solution, typically ethanol [6], prior to tryptic digestion, the purpose of which is to remove as many lipids and other interfering analytes from the tissues to reduce ion suppression. One approach to generating cell type–specific proteomic profiling from tissue sections is the integration of immunohistochemistry (IHC) staining, laser capture microdissection (LCM), and MS-based proteomics [7, 8]. This approach, where tissues are first stained to identify cell types of interest for microdissection and subsequent proteomics, has shown promising data with impressive cell type–specific protein numbers generated from areas as small as 0.2 mm^2 [8]. However, there are also limitations with using IHC as the spatial platform compared to MSI. First, molecular coverage is limited for IHC to proteins and protein complexes, while MSI can detect a range of different analyte classes [4, 5]. Second, IHC platforms are limited by the smaller number of unique species that can be detected in a single experiment. Often, IHC is performed with antibodies targeting only one or two proteins of interest simultaneously. Even more sophisticated multiplex platforms which report the ability to target as many as 40 + markers simultaneously pale in comparison to the profiling depth achieved by MSI [9]. Finally, the sample preparation cost and time required are significantly less for MSI compared to these platforms. Recently, many groups have replaced IHC with MSI as the spatial imaging platform for performing cell type–specific proteomics with LCM [10–17]. In this approach, the MSI data is used in an untargeted manner to generate regions of interest which are then dissected from either the same section or a serial section of the same tissue using LCM. These dissected subregions can then be homogenized, and the proteins extracted for digestion and analysis using LC–MS. This new workflow allows for the generation of high-dimensional multiomics data which can be combined to find changes in expression/abundance of multiple analyte classes. This approach is particularly useful for the study of diseases where tissue samples are highly heterogeneous such as PCa.

PCa is one of the most frequently diagnosed male malignancies and is critically dependent on androgens for growth and progression. This feature forms the basis of hormonal therapy being the standard of care for advanced disease [18]. Interestingly, one of the many cellular programs that androgens regulate in PCa is lipid metabolism, and it has been shown extensively in the literature that androgens induce de novo lipid synthesis in PCa cells [19, 20]. This lipogenic nature of PCa therefore makes it an excellent tissue model for MALDI-MSI lipidomics-guided LCM proteomics.

Materials and methods

Reagents and materials

α-Cyano-4-hydroxycinnamic acid (αCHCA), dithiothreitol (DTT), iodoacetamide (IA), and trifluoroacetic acid (TFA) were purchased from Sigma-Aldrich (MO, USA). Formic acid was acquired from ChemSupply Australia (SA, Australia). Trypsin and Superfrost Plus glass slides were purchased from Thermo Fisher Scientific (MA, USA). MS-grade methanol, water, and ammonium bicarbonate were supplied by Honeywell (NC, USA). RapiGest SF was bought from Waters Corporation (MA, USA). Indium-tin-oxide (ITO) coated conductive microscope slides were purchased from Bruker (Bremen, Germany), and polyethylene naphthalate (PEN) membrane microscope slides were purchased from Applied Biosystems (MA, USA). Lillie Mayer's hematoxylin and 1% alcoholic eosin were purchased from Hurst Scientific (WA, Australia).

Tissue sectioning

Ethical approval for the use of human prostate tumors from patients undergoing radical prostatectomy at the Royal Adelaide Hospital was obtained from the Ethics Committees of the University of Adelaide (Adelaide, Australia) (H-2018–222) and the Royal Adelaide Hospital (Adelaide, Australia) (041011). Fresh-frozen PCa biopsy cores were cryo-sectioned at − 18 °C on a Shandon Cryotome E (Thermo Fisher Scientific, MA, USA). For evaluation of PEN membrane slides for MSI experiments, cores from 10 patients were cut at 10 µm thickness and thaw mounted on ITO and PEN membrane slides. For combined MSI and LCM experiments, 9 patients were cut at 10 µm thickness and mounted onto PEN membrane slides. An additional 5-µm-thick section was placed on a Superfrost Plus microscope slide for each patient and used for H&E staining and pathology evaluation. After sectioning, slides were stored under nitrogen at − 80 °C until analysis.

Hematoxylin and eosin staining

Superfrost slides were thawed, and tissues first hydrated by submerging in running water followed by a 30-s stain with filtered Lillie Mayer's hematoxylin. Excess stain was removed by submerging in running tap water for 30 s

followed by differentiation in 0.5% acid alcohol for 4 s. Slides were returned to the running water until clear and then dipped in saturated aqueous sodium hydrogen carbonate for 10 s. After a final 30-s gentle wash in running water, the tissues were counterstained for 20 s in filtered 1% alcoholic eosin. Tissues were then dehydrated over 3 ethanol washes (3 min each) and cleared in xylene before being coverslipped using DPX mounting media.

MALDI-MSI sample preparation

PEN and ITO slides were prepared for imaging by first thawing in a vacuum desiccator for 30 min to prevent condensation. Fiducials were marked on each slide using correction fluid (whiteout, BIC) and allowed to dry. These marks were used to accurately align slide images throughout the workflow. Next, micrographs of the slides were made on a reflecta Tissue Scout scanner (Bruker Daltonics, Bremen Germany). The MALDI matrix, αCHCA, was applied at 7 mg/mL in 90:10:01 methanol:water:TFA (v/v/v) by auto-spraying with a Suncollect (Sunchrom GmbH Friedrichsdorf, Germany) system using the following method. A 3-mL plastic syringe (Henke-Sass, Wolf GmbH, Tuttlingen Germany) was used to deliver the matrix solution. A total of 15 layers were applied with a 30-s pause between each matrix layer at a *Z* position of 1 mm. The flow rate for the first 3 layers was 10 µL/min, 20 µL/min, and 30 µL/min followed by 40 µL/min for the remaining layers using an X-speed of low:5 and a Y-speed of Medium:1. Once the matrix was applied, the PEN membrane was punctured several times using a stainless-steel wire (*ca* 0.3 mm diameter). Holes were at least 4 mm away from any tissue. The perforation of the membrane was required to stop small air pockets from forming under the membrane at the reduced pressure of the MALDI source.

MALDI-MSI

Fresh-frozen PCa radical prostatectomy cores were imaged in positive ion mode on a timsTOF fleX mass spectrometer (Bruker, Bremen, Germany) using a 20 µm step- and pixel-size. Data was acquired between *m/z* 300–1300 at ~ 12–15 pixels/second. The Bruker SmartBeam™ 3D laser system was operated with 250 shots/pixel at 10 kHz and 50% laser energy. The MALDI plate offset and deflection delta voltages were optimized to 50 V and 70 V respectively while the funnel 1, funnel 2, and multipole RF voltages were set to 350 Vpp. The collision cell voltage was set to 10 V and the collision RF to 2500 Vpp. The transfer time between the collision cell and the time-of-flight (TOF) region was adjusted to 80 µs and the pre-pulse storage was set to 10 µs. The instrument detector was operated in focus mode. Tissues were imaged in a randomized order. Mass calibration was performed in ESI mode using direct infusion of sodium formate at a flow rate of 3 µL/min. A high precision calibration (HPC) was achieved with an accuracy of 100% and a standard deviation error of < 1 ppm. After MALDI-MSI the tissues were placed in a slide mailer. The mailer was flooded with nitrogen and sealed before being returned to − 80 °C storage until LCM.

MALDI-MSI data processing

To determine if PEN membrane slides were suitable for MALDI-MSI, MSI data were generated for $n = 10$ patients using both ITO and PEN membrane slides. The ITO and PEN data were imported into one SCiLS Lab file and pre-processed by normalization to total ion count (TIC), and setting the peak area processing width to 10 ppm. A feature list was generated for the combined dataset using the SCiLS Lab (2023b) feature finder tool using 30% coverage, 5% relative intensity, and weak spatial denoising. Univariate statistical tests (Wilcox Rank Sum) were performed on the 229 *m/z* features in SCiLS Lab with a significance threshold of $p = 0.05$. Tentative lipid identifications were made by searching *m/z* values through the LIPID MAPS database (lipidmaps.org), filtering for lipid species from the phosphatidylcholine (PC), sphingomyelin (SM), lysophosphatidylcholine (LPC), ceramide (CER), and acylcarnitine (CAR) subclasses using an adduct selection of $[M+H]^+$, $[M+Na]^+$, and $[M+K]^+$ with a 0.01 Dalton mass tolerance. For the combined MSI and LCM experiments, imaging data from the 9 patient samples were imported into a single SCiLS Lab file and normalized to TIC. An in-house lipid target list of 369 theoretical *m/z* values from commonly detected phosphatidylcholine (PC), lysophosphatidylcholine (LPC), and sphingomyelin (SM) species as H^+, Na^+, and K^+ adduct masses was imported and used for data processing and region definition (Online Resource 1). The list of 369 *m/z* values was then manually curated to remove any entries that did not yield a peak in the MS spectrum with s/n > 5:1 and a tissue-related spatial distribution. The curated list had 138 features and was used to spatially segment each tissue individually to define different cell types based on the MSI data. An interactive clustering approach using a bisecting *k*-means algorithm and correlation distance metric was used, and weak denoising was also applied. Regions of cancerous epithelia (CE), benign epithelia (BE), and stroma from each tissue were defined and saved as sub-regions by comparing the spatial segmentation maps to a co-registered and annotated H&E scan (Online Resource 2, Fig. S1).

Region mapping and LCM

The Bruker region mapper tool was used to facilitate the transfer of region of interest (ROI) coordinates from the SCiLS Lab landscape to the coordinate system of the Zeiss

PALM Robo LCM system (Oberkochen, Germany). A set of 3 teach marks per slide was identified in SCiLS Lab using the MALDI laser ablation marks left in the matrix. The teach mark/ROI data for each tissue was exported as a SCiLS exchange format file and imported into the Bruker region mapper. The tissues for dissection were then placed into the Zeiss LCM system after being thawed for 30 min in a desiccator. The corresponding teach mark locations used in the SCiLS lab were found under the LCM microscope using the MALDI laser ablation marks as a guide and "dot" elements were created from each. The LCM teach mark element list was imported into the region mapper software and ROI coordinate transfer was performed with high accuracy resulting in a residual root-mean-square error of < 1 µm. The Zeiss element list output files containing the mapped regions were then imported into the LCM for dissection. The Zeiss PALM Robo LCM system was operated using the AxioCam ICm1 camera for brightfield and laser capture. The laser cutting and catapulting parameters for both × 5 and × 20 magnification were optimized on tissue. For × 5 magnification dissection, a microbeam cut energy of 54% and 86% focus was used with an LMPC (laser pressure catapulting) energy of Δ55. For × 20 magnification cutting, the microbeam cutting energy was optimized for 46% with a 76% focus and an LMPC energy of Δ25. The distance between LMPC shots for all dissection methods was 30 µm. For each tissue, the mapped regions were imported, and the cut method was set to CentreRoboLPC. Regions less than 1600 μm^2 were removed from the element list. Dissected regions from each patient and cell type group were captured into clean 600 µL tube caps (Thermo Fisher Scientific, MA, USA) with 20 µL of MS-grade water used as a capture solution. Tissue areas not dissected successfully at × 20 magnification were re-cut at × 5 magnification. Ten microliters of MS-grade water was added to each tube cap after capture and samples were immediately placed on ice. A short 20-s centrifugation was performed to collect cell material and capture solution to the bottom of the tubes prior to storage at − 80 °C. A total of 17 samples from 9 patients were captured for proteomics analysis.

Nano-LC–MS/MS proteomics

All samples were thawed from − 80 °C on ice and prepared simultaneously. To the 30 µL of capture solution from each sample, 14 µL of 25 mM ammonium bicarbonate and 2.5 µL of 1% Rapigest SF (1 mg dissolved in 100 µL of 25 mM ammonium bicarbonate) (0.05% final concentration) were added and sonicated before heating at 80 °C for 10 min. To reduce cysteine-cysteine disulfide bonds, 1.3 µL of 100 mM DTT was added (final concentration of 2.5 mM) and briefly vortexed. The samples were heated for 10 min at 60 °C and then allowed to cool to room temperature before spinning at low speed to collect the condensate at the bottom of the tube. As an alkylating agent, 1.3 µL of IA (7.5 mM final concentration) was added and mixed by briefly vortexing. The samples were incubated in the dark at room temperature for 30 min. A 0.2 µL aliquot of trypsin (1:100 w/w, 10 µg) was added and the mixture was incubated for 16 h at 37 °C with gentile agitation using an Eppendorf thermomixer (Hamburg, Germany). After the tryptic digestion step, the samples were centrifuged at 13,000 × g (Heraeus BioFuge Pico, Thermo Fisher Scientific, MA, USA) for 30 min and the supernatant retained. TFA was added for a final concentration of 0.5% and incubated for 40 min at 37 °C. A final centrifugation at 13,000 × g for 10 min was performed and the supernatant containing tryptic peptides was retained. C18 StageTips were used for sample cleanup as previously reported [21]. The tips were conditioned by first loading and eluting 50 µL of 100% acetonitrile followed by equilibration with 50 µL of 0.1% TFA. All 50 µL of the sample was then loaded into the tip and washed with an additional 50 µL of 0.1% TFA. Finally, the bound peptides were eluted into a clean tube using 50 µL of 50% acetonitrile with 0.1% TFA. The peptides were dried overnight before being reconstituted in 40 µL of 0.1% formic acid. Proteomics experiments were performed using the same Bruker timsTOF fleX instrument used for MALDI-MSI equipped with a captive spray source and an Acquity M-Class nano-LC system (Waters Corporation MA, USA). LC separation was performed using a trap elute method; peptides were loaded onto a Symmetry C18 (180 µm × 20 mm) trap column (Waters Corporation MA, USA) for 5 min with 0.1% TFA at 10 µL/minute. Peptides were then eluted and chromatographically separated using an Aurora Series column with CSI, Gen2 (25 cm × 75 µm ID, 1.6 µm C18) (Ion Opticks, Melbourne Aus.) held at 50 °C and gradient elution with mobile phase A water and mobile phase B acetonitrile both containing 0.1% formic acid. The flow rate was set to 400 nL/minute; mobile phase B was increased from 1 to 17% over 60 min before increasing to 25% over a further 30 min. The gradient was increased from 25 to 37% over 10 min and then to 95% over another 10 min. The gradient was held at 95% for 10 min and then returned to starting conditions (1% B) for 10 min before the next sample injection was commenced. Mass calibration was performed using sodium formate in HPC calibration mode while mobility calibration was performed in linear calibration mode using three Tune Mix ions at theoretical masses of *m/z* 622.0290, *m/z* 922.0098, and *m/z* 1221.9906. Data was acquired in positive ion mode between *m/z* 100 and 1700 using the dia-PASEF scan mode. A custom trapped ion mobility separation (TIMS) method was used to separate ions with mobilities from 0.6 to 1.60 V.s/cm^2 using a 100 MS ramp and accumulation time. This separation method resulted in a 100% duty cycle and ramp rate of 9.52 Hz. The transfer of peptide ions in the mass range of *m/z* 100–1700

was optimized. The deflection delta was set to 70 V and the funnel 1, funnel 2, and multipole RF voltages were adjusted to 475 Vpp, 200 Vpp, and 200 Vpp respectively with a 1500 Vpp collision RF. The collision energy settings for dia-PASEF acquisition were 20 eV at 0.85 V.s/cm^2 and 59 eV at 1.30 V.s/cm^2. For optimal detection, the transfer duration between the collision cell and the TOF was set to 60 µs with a 12 µs pre-pulse storage.

Proteomics data processing

dia-PASEF data was pre-processed and protein identification was performed using DIA-NN**.** Precursor ion searching was performed for trypsin/P protease digestions with 1 missed cleavage allowed with the following modifications permitted: N-term M Excision, C Carbamidomethylation, and Ox(M). A precursor FDR rate of 1% was used and match between runs (MBR) was selected for batch processing. Protein names were converted to gene names and the data was uploaded to Metaboanalyst [22] for further statistical analysis. The output from DIA-NN containing the table of protein accession numbers, converted gene names, and intensity values for each LC–MS sample can be found in Online Resource 3. In Metaboanalyst, features with > 15% missing values from all samples were removed, and the remaining missing values were imputed using the *K*-nearest neighbors (KNN) (feature-wise) method. This threshold was selected to prevent features present in one group exclusively from being removed. Peak intensities were then quantile-normalized, log10-transformed, and auto-scaled. A principal component analysis was performed on the scaled data and differentially abundant proteins were identified by a two-sample *t*-test using an intensity fold-change threshold of 1.5 and false discovery rate (FDR) threshold of 0.1. The fold change of each individual protein was exported from Metaboanalyst and then imported into R 4.2.0. Enrichment analysis was performed using the fgsea package (v1.22.0) with feature sets from the molecular signatures database (mSigbDB) as implemented in msigdbr (v7.5.1). Significantly enriched sets were identified using an FDR threshold of 0.05. Plots of enriched sets were plotted in R using ggplot2 (v3.3.6) and ComplexHeatmap (v2.12.0). The full enrichment analysis results including pathway information, significance values, and feature contributions for each pathway can be found in Online Resource 4.

Results and discussion

MALDI-MSI sensitivity on PEN membrane slides

Conductive ITO slides are used in MALDI-MSI to provide an electrically conductive surface that can reduce unwanted charging effects and assist in the acceleration of ions in the ion source [23]. This is particularly important in axial geometry time-of-flight (TOF) instruments where the sample holder is part of the ion source and the mass analyzer. To determine whether non-conductive PEN membrane slides are compatible with MALDI-MSI in an orthogonal acceleration TOF, data acquired from serial sections of $n = 10$ patient samples mounted on ITO and PEN membrane slides were compared. From the 229 features detected in all samples, 90 had significantly different mean intensities between the ITO and PEN membrane–mounted tissues (Wilcoxon rank-sum corrected $p < 0.05$). When searched against the LIPID MAPS database, 27 of these features were tentatively identified as lipids based on their exact *m/z* (3 LPCs, 11 SMs, and 13 PCs) (Online Resource 2**,** Table S1). Figure 1 shows the distribution and relative intensity of 3 ions in serial sections mounted on ITO and PEN slides respectively. The ions measured at *m/z* 518.3221 and *m/z* 826.5718 tentatively assigned as predominantly LPC 16:0 $[M + Na]^+$ and PC 36:1 $[M + K]^+$ (Fig. 1a and b) are localized to the BE glands of the prostate while the ion measured at *m/z* 772.5255 tentatively assigned as predominantly the $[M + Na]^+$ adduct of PC 32:0 (Fig. 1c) was detected more in the STR areas. When comparing the ion distributions between the ITO and PEN membrane–mounted tissues, the localization and intra-tissue intensity show a high degree of similarity. For example, whereas the *absolute* intensity on the PEN slide is lower than ITO, the *relative* intensity difference between epithelia and stroma for LPC 16:0 and PC 36:1 (Fig. 1a and b) is comparable for both slide types. Critically, hierarchical clustering of spatially resolved MS data produced nearly identical segmentation maps regardless of slide type, and both these maps were structurally similar to serial H&E-stained sections (Fig. 1d). This is fundamental to the proposed workflow as it ensures that specific cell types are selected for dissection and proteomic analysis. As expected, ITO slides yielded higher ion intensities in MALDI-MSI experiments. However, LCM is typically performed using PEN membrane slides [24]. These non-conductive microscope slides are covered in a polyethylene naphthalate membrane, which facilitates optimal LCM performance. While non-membrane slides can be used for LCM, a reduction in tissue recovery is observed. This was highlighted by Mezger and colleagues who reported a significant decrease in protein identifications when comparing equal areas of dissected rat cardiac tissue from serial sections mounted on PEN and ITO slides [13]. Based on our observations, PEN slides are the best choice for combined spatial lipidomics/LCM proteomics workflow. Although signal intensity for lipid imaging using these slides was reduced, no alteration in spatial segmentation or loss of lipidome coverage was observed.

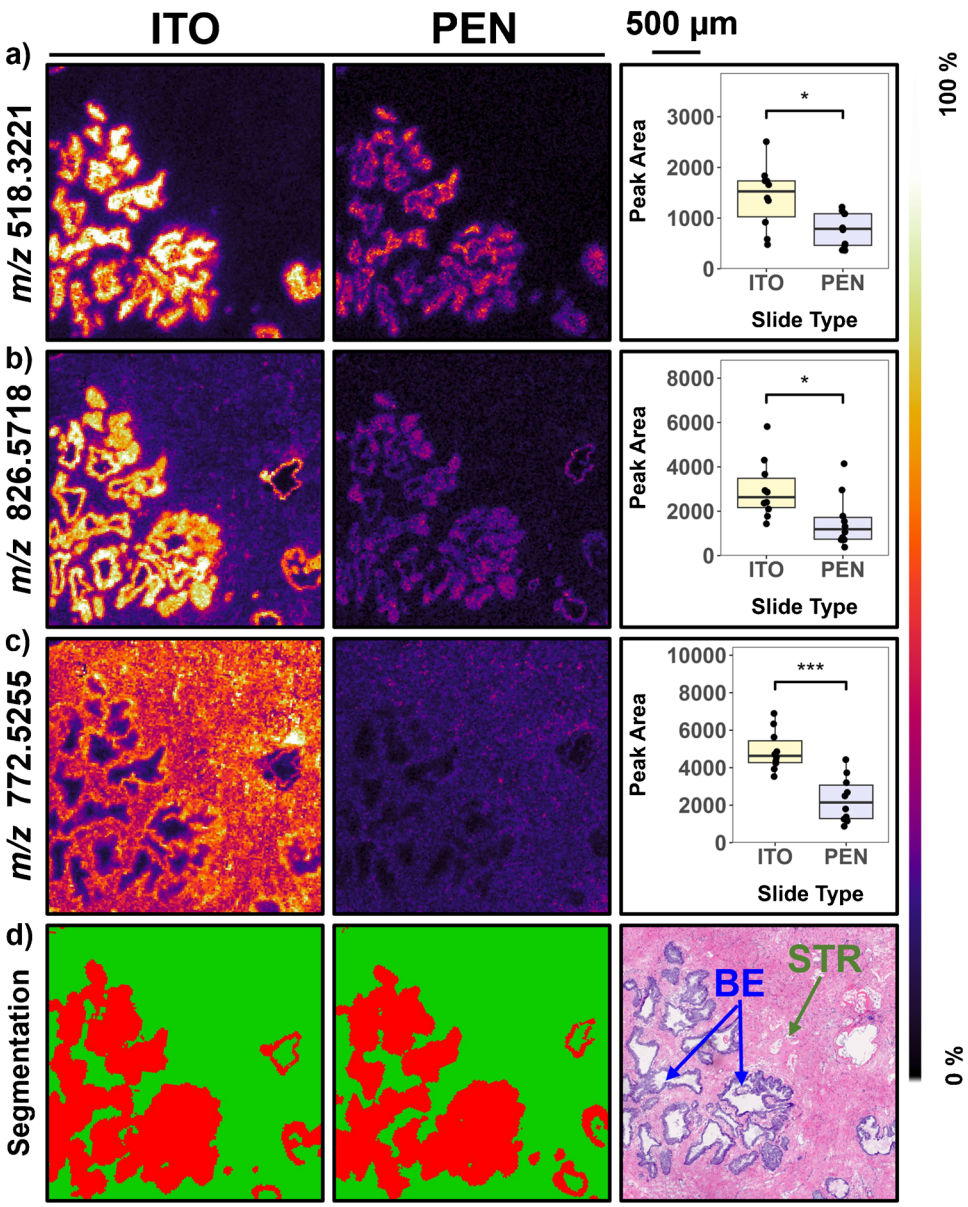

Fig. 1 MSI data comparing sensitivity between prostate tissues prepared and imaged on ITO and PEN membrane slides. Change in relative intensity between ITO and PEN membrane mounted samples for 3 abundant ions detected in positive ion mode tentatively assigned as **a** LPC 16:0 $[M+Na]^+$, **b** PC 36:1 $[M+K]^+$, and **c** PC 32:0 $[M+Na]^+$. Boxplots in the right column show average peak areas for all samples (WRS corrected $p<0.05$). **d** Spatial segmentation maps generated through bisecting *k*-means clustering on ITO and PEN membrane–mounted tissues. The color scale bar shows relative intensity

Lipidomics-driven segmentation and LCM mapping

ROIs for dissection and proteomics analysis were defined in the MSI data by comparing the lipidomics-driven bisecting *k*-means segmentation with serial H&E-stained and annotated sections. The segmentation maps and annotated H&E images for all samples included in the analysis can be found in Online Resource 2, Fig. S1. The largest lipidomic difference between regions of CE and BE in our data appeared to be the relative increase of several LPC species in regions of BE and an increase in several PC species in regions of CE (Online Resource 5). These observations are consistent with previous MSI studies in PCa that have identified LPCs, namely LPC 16:0 as being associated with benign lesions [25, 26] and even predictive of biochemical relapse [26], as well as PC species such as the dominant PC 34:1 being associated with cancerous lesions of the prostate [27]. Accurate transfer of ROI coordinates from the MSI data to the LCM instrument is a key step that ensures that the tissue harvested is from the tissue type of interest with minimal contamination from neighboring regions. This results in proteomics data that is derived purely from that tissue type. To achieve maximum accuracy in our workflow, we used the SCiLS Region Mapper tool (v0.1) to transfer coordinates from the SCiLS Lab landscape to the coordinate system of the Zeiss PALM Robo LCM. The Region Mapper software requires 3 "teachmark" coordinates to be identified in both the MSI data and in the tissue under the LCM microscope for coordinate transfer. Similar to the approach reported by Eiersbrock and colleagues [28], we used the ablation marks

left in the matrix by the MALDI laser to enhance the accuracy and reproducibility of coordinate mapping as these marks are highly distinctive (Fig. 2). Pixels in the SCiLS Lab file on the periphery of the acquired region spaced roughly equidistant (Fig. 2a, b, and c) were used as "teachmark" locations as they were easy to identify under a microscope. The accuracy of this approach is demonstrated in Online Resource 2, Fig. S2. Figure S2a shows the segmentation map of a prostate tissue with 4 clusters and Fig. S2b shows the camera view from the LCM instrument after the region corresponding to the yellow cluster had been dissected. An overlay of the two images highlights the accuracy of the region mapping and dissection achieved (Fig. S2c). While previous work has shown high-accuracy mapping using in-house MATLAB scripts [11, 13], manual image scaling with ImageJ [28], or online open-source platforms like Scilab [10], the method presented here uses an extension of SCiLS Lab with an intuitive graphical user interface which provides a seamless, reproducible, and accurate method for users of SCiLS Lab that does not require extensive knowledge of MATLAB or image processing tools.

Proteomic profiling of distinct tissue areas in prostate cancer samples

Nano-LC–MS/MS proteomics was performed on 6 benign epithelial, 6 stromal, and 5 cancerous epithelial regions using a dia-PASEF workflow on the same timsTOF fleX

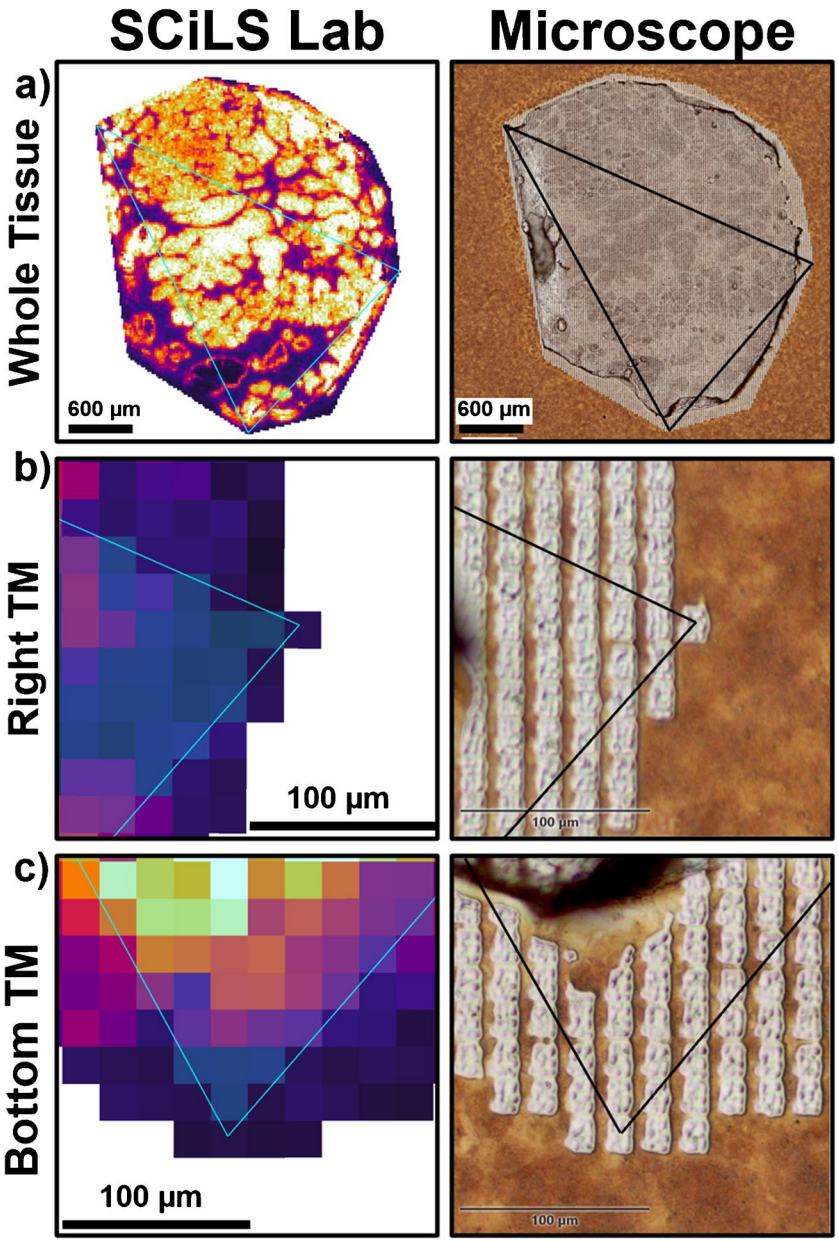

Fig. 2 ROI coordinate mapping and transfer using the SCiLS Lab region mapper tool. **a** 3 pixels were identified and selected as vertices for the teachmark region in the SCiLS Lab landscape and underneath a microscope. **b**, **c** The MALDI laser ablation marks left in the matrix and individual data pixels were used as vertices to achieve high-accuracy teaching. TM = teachmark

mass spectrometer used for MSI experiments. Despite the tissues being previously irradiated by the MALDI laser, a total of 5525 protein groups were identified across all samples with a 1% FDR threshold (Online Resource 3). Figure 3a shows the number of protein groups identified across samples from the 3 tissue types. The average number of protein groups identified from regions of BE, CE, and STR were 4553, 4406, and 4482 respectively. The largest area dissected had an area of 15.63 mm^2 and resulted in 5131 protein IDs while 3316 proteins were identified from the smallest region dissected at 1.75 mm^2. A full list of dissected sample sizes and protein numbers can be found in Online Resource 2, Table S2. These results are comparable to previous reports of LCM proteomics on imaged tissues mounted on PEN membrane slides. Dewez and colleagues [11] reported 1426 total proteins from dissected breast cancer tissues as small as 0.3 mm^2 while Dilillo et al. [10] in their analysis of 1 mm^2 mouse brain regions were able to detect up to 2170 unique proteins. MetaboAnalyst was used to evaluate the performance of our method by finding changes in protein expression associated with each tissue type that were consistent with previous reports in the literature. A principal component analysis (PCA) was performed to identify the most variance in the data set. Consistent with highly accurate region excision during the LCM step, the samples labelled CE, BE, and STR separated from each other along the first 2 principal components with 30.4% and 11.6% variance explained by PC1 and PC2 respectively (Fig. 3b). To further confirm the accuracy and specificity of the region mapping and dissection process, proteins significantly enriched between the CE

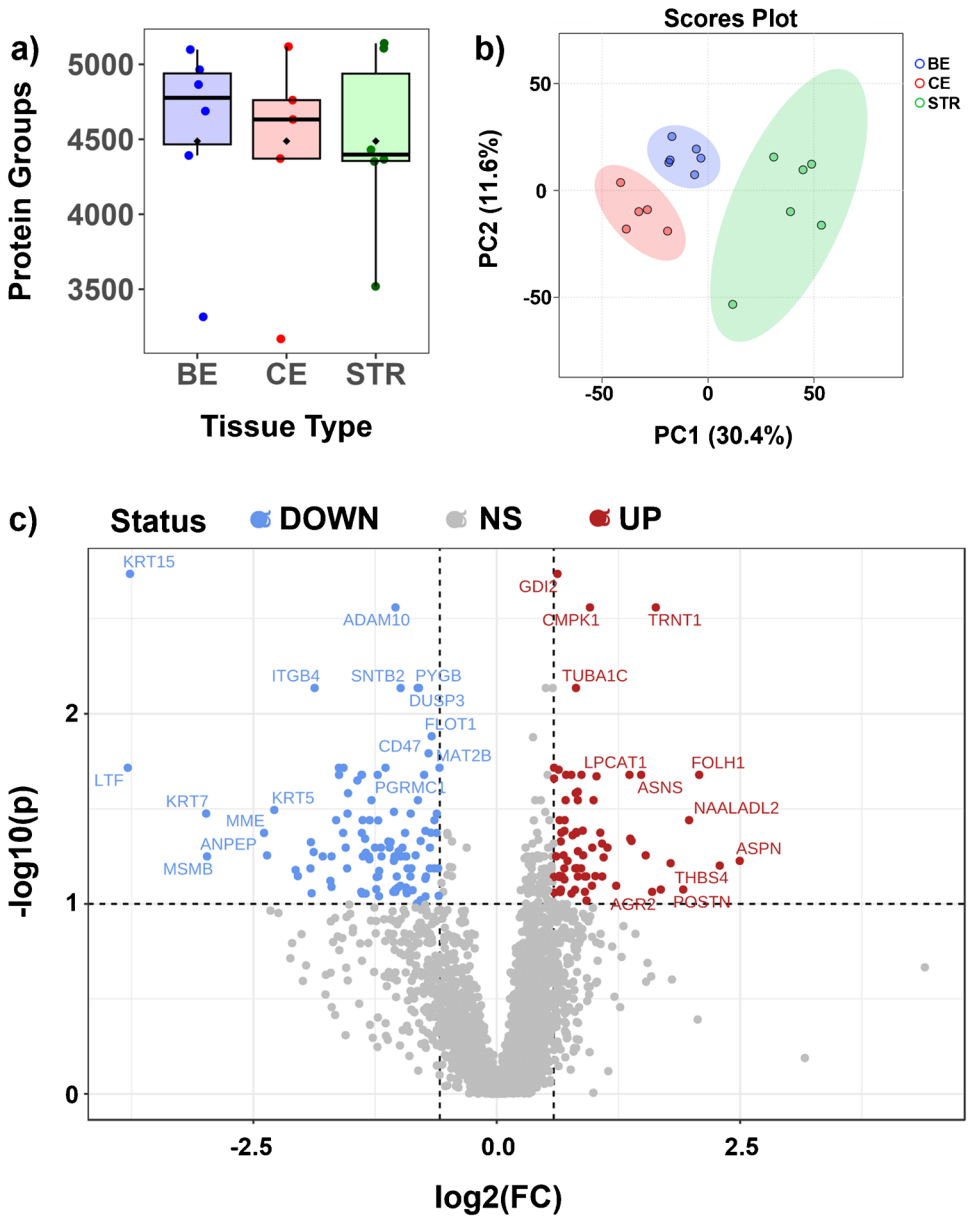

Fig. 3 Proteomic profiling of distinct tissue types dissected and analyzed using LCM and dia-PASEF nano-LC/MS. **a** Boxplot of protein groups from 6 regions of BE, 6 regions of STR, and 5 regions of CE. Black diamond represents group mean. **b** PCA scores plot showing the clustering of samples colored by tissue type along PC1 and PC2. **c** Volcano plot of proteins differentially expressed between the CE and BE. Direction of comparison = CE/BE. FDR *p*-value threshold = 0.1. FC threshold = 1.5

and BE samples were identified using a two-sample *t*-test. In our analysis, we found 74 proteins significantly increased and 107 proteins significantly decreased in cancerous compared to benign epithelia using a fold-change threshold of 1.5 (50% increase in signal intensity) and a *p*-value 0.1 (FDR) (Fig. 3c).

We next sought to test whether the overall proteomic changes were consistent with prostate cancer biology and the prior literature by adapting an analysis procedure from transcriptomics, gene set enrichment analysis. This approach takes as input a list of genes and their rank (in this case, protein fold change between cancerous and benign was used as input) and then tests whether a pre-defined subset of this list has a non-random distribution. Using this approach, with pre-defined sets supplied by the Molecular Signatures Database (mSigDB), we identified > 450 sets which were significantly different between conditions (FDR < 0.05, Online Resource 4). The most significant enrichment signature was downregulation of immune functions within cancerous tissue relative to benign (Fig. 4). Prostate cancer is well known to be an immunologically "cold" form of cancer [29] with little immune infiltration, and as such a lower level of immune-related expression in cancerous tissue relative to benign may be expected. Additionally, the top upregulated sets were all from prior prostate cancer datasets [30–32] indicating that the changes we observed with this methodology are in line with what has been previously reported. We also observed downregulation of multiple sets related to KRAS signalling (Fig. 4), which is frequently mutated in prostate cancer. Our differential protein analysis reflects the precision of the lipidomics-driven segmentation, region mapping, and the dissection process. Surprisingly, p63, a p53-related protein encoded by the *TP63* gene, was not detected in any of our samples. p63 is involved in cell proliferation, differentiation, and apoptosis [33, 34]. In prostate tissues, it is strongly expressed by the basal epithelium, a one-cell thick layer of epithelia that separates the prostatic stroma from the luminal epithelium. Upon progression to prostate adenocarcinoma, this basal cell layer is lost, a feature which is often used as a diagnostic indicator by pathologists [35]. The absence of p63 not only from the CE samples but also from the BE regions highlights a potential limitation with this workflow as the data-driven segmentation separated the benign and cancer glands from the surrounding stroma. This means region borders coincide with the basal epithelium cell layer. As the entire areas from both the benign and cancerous glands were dissected, it is possible that the absence of detectable p63 in our dataset is the result of the basal cell layer being destroyed by the LCM laser during excision.

LPCAT1 expression and LPC/PC ratio

A large network of lipogenic enzymes has been identified and characterized in human disease [36]. While some of these enzymes are enriched in many cancers and influence the lipidome more broadly, such as fatty acid synthase (FASN) [37], or acetyl-coA carboxylase (ACC1) [38], there are many enzymes that have more specific functions which can be reflected in the spatial lipidomics data. Lysophosphatidylcholine acyltransferase 1 (LPCAT1) is a protein that is overexpressed in many cancers including liver, gastric, and prostate [39, 40]. This protein exhibits acyltransferase

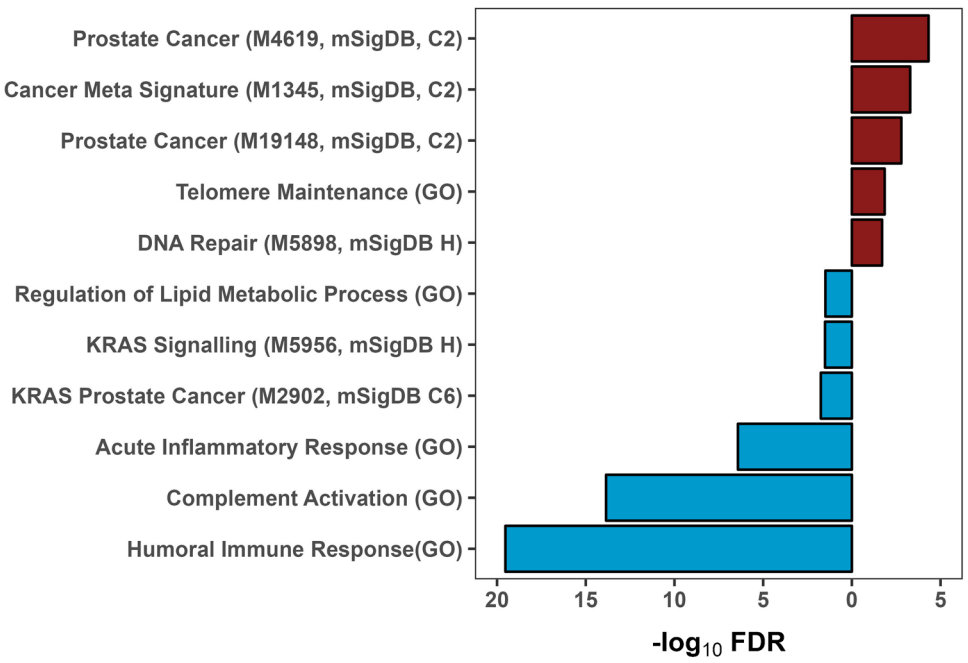

Fig. 4 Selected molecular signatures database (mSigDB) gene sets and gene ontology (GO) terms enriched among differentially expressed proteins (DEPs) in cancerous tissue compared to benign. Enrichment analysis carried out with the *fgsea* package in R

activity and is responsible for the conversion of LPCs to PCs via the remodelling pathway of the Lands cycle [41]. More specifically, in PCa, LPCAT1 overexpression has been associated with tumor grade and progression after treatment of primary disease [42, 43]. In our dataset, LPCAT1 was detected in both the benign and cancerous glands; however, it was significantly enriched in the CE samples ($p = 0.02$, log2 FC = 1.36) (Fig. 5a) which is consistent with these reports. More recently, a comprehensive analysis of the LPCAT1 function by Zhao and colleagues [44] using isomer-resolved tandem MS revealed that LPCAT1 exclusively operates at the *sn*-1 position and therefore uses only *sn*-2 LPCs as precursors. In addition, using PC 0/16:0 (LPC 16:0) as the precursor for their experiments, they were able to show that while the *sn*-1 selectivity of LPCAT1 was independent of the fatty acyl donator, there did appear to be a greater reaction rate for saturated and monounsaturated fatty acids compared to polyunsaturated fatty acids, a finding that has also been reported independently [45]. To investigate the activity of LPCAT1 in the spatial lipidomics data, we visualized the relative abundance of LPCAT1 using the protein intensity from each dissected region (Fig. 5b) and compared it to ion intensity ratio images of PC 34:1/LPC 16:0 and PC 32:1/LPC 16:0 lipid pairs (Fig. 5d, f). We found that LPC 16:0 was localized to the BE regions in our imaging data (Online Resource 2, Fig. S3a), which is consistent with other MSI studies in PCa [25, 26], and that a decreased relative abundance of LPCAT1 was also in these regions after dissection. Figure 5 shows the correlation between LPCAT1 expression and the ratio of LPC 16:0 $[M+K]^+$ and its potential products PC 34:1 (Fig. 5c, d) and PC 32:1 (Fig. 5e, f). For each PC/LPC pair, the ion intensity ratio (PC/LPC $[M+K]^+$) was significantly higher in the CE than in the BE (two-sample *t*-test, $p < 0.05$) (Fig. 5c, e). This effect was visualized by displaying these ion intensity ratios (Fig. 5d, f). The $[M+H]^+$ and $[M+Na]^+$ adducts of different PC lipids are near isobaric and cannot readily be separated in MSI experiments. For this reason, we chose to use $[M+K]^+$ ions in this work, thus greatly reducing isobaric interference [46]. The ratio ion images in Fig. 5 show an increase of PC 34:1 (predominantly reported as containing an 18:1 and 16:0 fatty acid [47] and confirmed through LC–MS/MS [data not shown]) and PC 32:1 (predominantly PC 16:1/16:0 [data not shown]) in the CE region of a prostate tissue section compared to the BE; furthermore, the ratio ion images for those lipid pairs show a similar localization to the LPCAT1

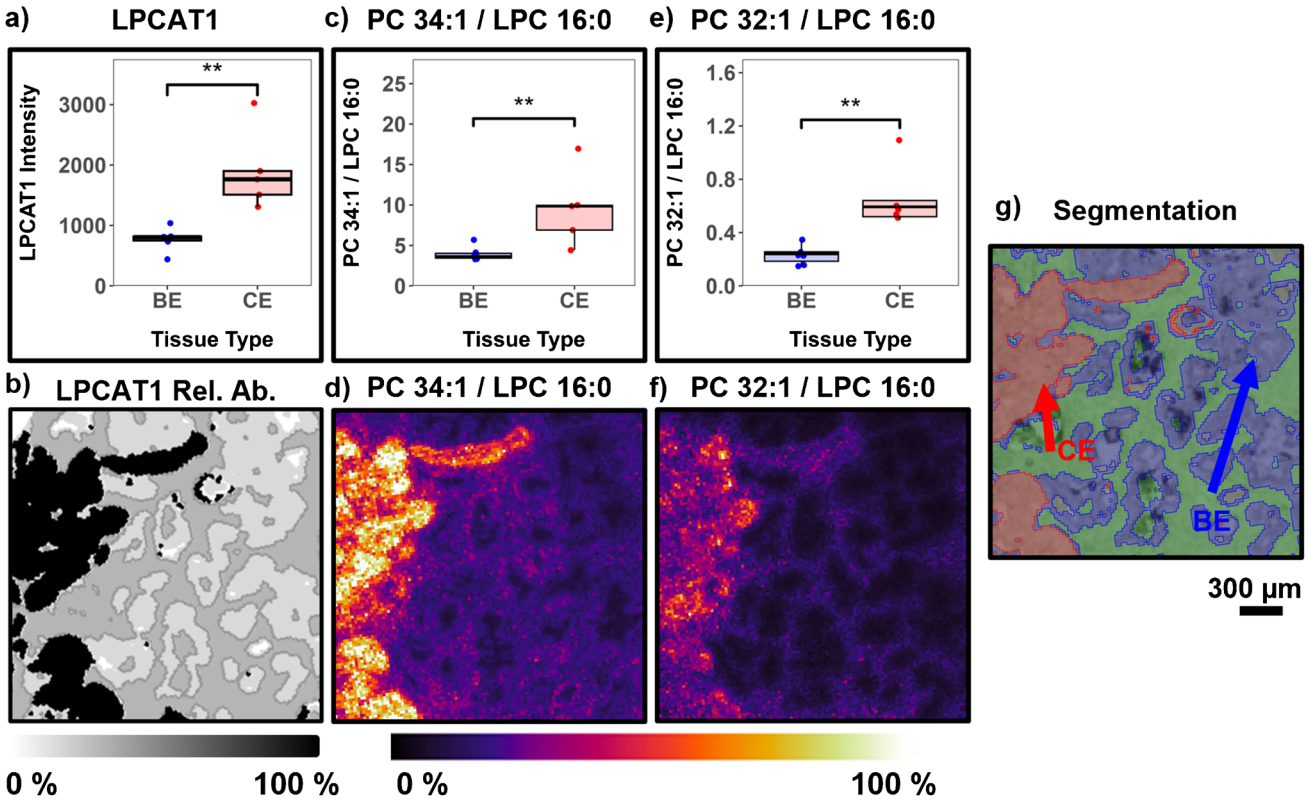

Fig. 5 **a** Intensity boxplot of protein LPCAT1 intensity in CE and BE regions. **b** LPCAT1 relative intensity image. Boxplots of the intensity ratio of **c** PC 34:1/LPC 16:0 and **e** PC 32:1/LPC 16:0. **d**, **f** Ratio ion images of each PC/LPC pair generated by normalizing to LPC 16:0 peak area. Significance reported as *p*-value of two-sample *t*-test ($p < 0.05$). Physical scale bar indicates 300 µm. **g** Segmentation map of a prostate tissue section showing regions of BE (blue), CE (red), and STR (green). Rel.Ab. = relative abundance

relative intensity image (Fig. 5b). These results are consistent with LPC 16:0 being a substrate for LPCAT1 [44] and with the enrichment of the protein detected in our dissected CE samples. However, it should be noted that we are unable to distinguish between *sn*-1 and *sn*-2 LPC lipids. Furthermore, independent reports of LPCAT1 protein expression by IHC and LPC 16:0 distribution measured by MALDI-MSI have linked these factors to PCa relapse [26, 42, 43], highlighting the potential for this technique to be incorporated into spatial multiomic biomarker discovery settings. Interestingly, however, we observed that the likely products of LPCAT1 activity on LPC 16:0 had different localizations. For example, the TIC normalized ion image of PC 32:1 $[M+K]^+$ appeared to be localized to the CE regions while the TIC normalized ion image of PC 34:1 $[M+K]^+$ was detected consistently in both BE and CE regions with higher relative intensities in the CE (Online Resource 2, Fig. S3). This highlights the fact that the synthesis of PC lipids can occur through both the remodelling pathway of the Lands cycle and the Kennedy pathway [41], and that specific fatty acids may be used in cancerous tissue by a certain pathway that is not typically observed or active in benign lesions. Alternatively, this feature of our MSI data could be the result of unresolved isomeric contributions. For example, the intensity from PC 34:1 $[M+K]^+$ which appears to be localized to both BE and CE areas most likely contains contributions from PC 18:1/16:0 and PC 16:0/18:1. Indeed, Zhao and colleagues [44] show in their work using isomer-resolved DESI MSI that PC 18:1/16:0, the product of LPC 16:0 conversion by LPCAT1, was associated with LPCAT1 expression by IHC and was highly localized to the tumor area of hepatocellular carcinoma tissues while the isomer PC 16:0/18:1, which would be the product of LPC 18:1 given the strict *sn*-1 specificity of LPCAT1, was localized to the benign regions [44]. Therefore, it is reasonable to assume that the peak measured at *m/z* 798.5415 assigned as PC 34:1 $[M+K]^+$ in our data is a combination of both these lipids. This highlights how integration and interpretation of multiomics datasets generated using this approach are dependent on the profiling depth of the individual omics platforms.

Conclusion

In this work, we have demonstrated the generation of spatial multiomics data from clinical PCa tissues using MALDI-MSI and LCM proteomics. PEN membrane slides were evaluated and found to be the best sample support for the full workflow striking a compromise between optimal LCM and acceptable lipid MSI performance. High-accuracy region mapping and precise tissue dissection were achieved using the Bruker region mapper software. This workflow streamlines the integration of spatial lipidomics with LCM proteomics using the same software for image segmentation and LCM region definition. Bottom-up proteomics performed on dissected samples revealed differentially abundant proteins that were consistent with the labelling of CE and BE regions. Finally, the activity of a lipogenic enzyme LPCAT1 previously reported in PCa was visualized in the MALDI-MSI data as an increase in the ratio of PC 34:1 and PC 32:1 to its precursor LPC 16:0 in CE compared to BE regions.

Supplementary Information The online version contains supplementary material available at https://doi.org/10.1007/s00216-024-05178-z.

Acknowledgements The authors would like to acknowledge all those involved with the collection and storage of tissues as part of the Australian Prostate Cancer BioResource (APCB) and the men who donated their tissue for research.

Author contribution The manuscript was written through the contributions of all authors. / All authors have given approval to the final version of the manuscript. The methodology described was established by J. X. M. Truong, P. J. Trim, M. F. Snel, L. M. Butler, and S. R. Rao. Data analysis was performed by J. X. M. Truong, P. J. Trim, M. F. Snel, and F. J. Ryan.

Funding The instrument used in this research is located in the Australian Cancer Research Foundation (ACRF) Centre for Integrated Systems Biology at the South Australian Health and Medical Research Institute (SAHMRI) and was funded by the ACRF. J. X. M. Truong is supported by a Postgraduate Scholarship from both the University of Adelaide and the Freemasons Centre for Male Health and Wellbeing.

Data availability Available on request.

Code availability Available on request.

Declarations

Ethics approval Ethical approval for the use of human prostate tumors was obtained from the Ethics Committees of the University of Adelaide (Adelaide, Australia) (H-2018–222) and the Royal Adelaide Hospital (Adelaide, Australia) (041011).

Consent to participate Not applicable.

Consent for publication Not applicable.

Conflict of interest The authors declare no competing interests.

References

1. Shuken SR. An introduction to mass spectrometry-based proteomics. J Proteome Res. 2023;22(7):2151–71.
2. Hsu FF. Mass spectrometry-based shotgun lipidomics - a critical review from the technical point of view. Anal Bioanal Chem. 2018;410(25):6387–409.
3. Zhu S, Chen J, Zeng H. Our current understanding of the heterogeneity in prostate cancer and renal cell carcinoma. J Clin Med. 2023;12(4):1526.
4. Djambazova KV, Klein DR, Migas LG, Neumann EK, Rivera ES, Van de Plas R, et al. Resolving the complexity of spatial

lipidomics using MALDI TIMS imaging mass spectrometry. Anal Chem. 2020;92(19):13290–7.
5. Mutuku SM, Trim PJ, Prabhala BK, Irani S, Bremert KL, Logan JM, et al. Evaluation of small molecule drug uptake in patient-derived prostate cancer explants by mass spectrometry. Sci Rep. 2019;9(1):15008.
6. Guo G, Papanicolaou M, Demarais NJ, Wang Z, Schey KL, Timpson P, et al. Automated annotation and visualisation of high-resolution spatial proteomic mass spectrometry imaging data using HIT-MAP. Nat Commun. 2021;12(1):3241.
7. Huang P, Kong Q, Gao W, Chu B, Li H, Mao Y, et al. Spatial proteome profiling by immunohistochemistry-based laser capture microdissection and data-independent acquisition proteomics. Anal Chim Acta. 2020;1127:140–8.
8. He J, Zhu J, Liu Y, Wu J, Nie S, Heth JA, et al. Immunohistochemical staining, laser capture microdissection, and filter-aided sample preparation-assisted proteomic analysis of target cell populations within tissue samples. Electrophoresis. 2013;34(11):1627–36.
9. Tan WCC, Nerurkar SN, Cai HY, Ng HHM, Wu D, Wee YTF, et al. Overview of multiplex immunohistochemistry/immunofluorescence techniques in the era of cancer immunotherapy. Cancer Commun (Lond). 2020;40(4):135–53.
10. Dilillo M, Pellegrini D, Ait-Belkacem R, de Graaf EL, Caleo M, McDonnell LA. Mass spectrometry imaging, laser capture microdissection, and LC-MS/MS of the same tissue section. J Proteome Res. 2017;16(8):2993–3001.
11. Dewez F, Martin-Lorenzo M, Herfs M, Baiwir D, Mazzucchelli G, De Pauw E, et al. Precise co-registration of mass spectrometry imaging, histology, and laser microdissection-based omics. Anal Bioanal Chem. 2019;411(22):5647–53.
12. Mezger STP, Mingels AMA, Soulié M, Peutz-Kootstra CJ, Bekers O, Mulder P, et al. Protein alterations in cardiac ischemia/reperfusion revealed by spatial-omics. Int J Mol Sci. 2022;23(22):13847.
13. Mezger STP, Mingels AMA, Bekers O, Heeren RMA, Cillero-Pastor B. Mass spectrometry spatial-omics on a single conductive slide. Anal Chem. 2021;93(4):2527–33.
14. Dewez F, Oejten J, Henkel C, Hebeler R, Neuweger H, De Pauw E, et al. MS imaging-guided microproteomics for spatial omics on a single instrument. Proteomics (Weinheim). 2020;20(23):e1900369-n/a.
15. Claes BSR, Krestensen KK, Yagnik G, Grgic A, Kuik C, Lim MJ, et al. MALDI-IHC-guided in-depth spatial proteomics: targeted and untargeted MSI combined. Anal chem (Washington). 2023;95(4):2329–38.
16. Longuespée R, Alberts D, Baiwir D, Mazzucchelli G, Smargiasso N, De Pauw E. MALDI imaging combined with laser microdissection-based microproteomics for protein identification: application to intratumor heterogeneity studies. Methods in molecular biology (Clifton, NJ). 2018;1788:297–312.
17. Alberts D, Pottier C, Smargiasso N, Baiwir D, Mazzucchelli G, Delvenne P, et al. MALDI imaging-guided microproteomic analyses of heterogeneous breast tumors—a pilot study. Proteomics Clin Appl. 2018;12(1):1700062.
18. Litwin MS, Tan H-J. The diagnosis and treatment of prostate cancer: a review. JAMA, J Am Med Assoc. 2017;317(24):2532–42.
19. Zadra G, Ribeiro CF, Chetta P, Ho Y, Cacciatore S, Gao X, et al. Inhibition of de novo lipogenesis targets androgen receptor signaling in castration-resistant prostate cancer. Proc Natl Acad Sci USA. 2019;116(2):631–40.
20. Swinnen JV, Esquenet M, Goossens K, Heyns W, Verhoeven G. Androgens stimulate fatty acid synthase in the human prostate cancer cell line LNCaP. Can Res. 1997;57(6):1086–90.
21. Rappsilber J, Mann M, Ishihama Y. Protocol for micro-purification, enrichment, pre-fractionation and storage of peptides for proteomics using StageTips. Nat Protoc. 2007;2(8):1896–906.
22. Xia J, Psychogios N, Young N, Wishart DS. MetaboAnalyst: a web server for metabolomic data analysis and interpretation. Nucleic acids research. 2009;37(suppl-2):W652–60.
23. Scherl A, Zimmermann-Ivol CG, Dio JD, Vaezzadeh AR, Binz P-A, Amez-Droz M, et al. Gold coating of non-conductive membranes before matrix-assisted laser desorption/ionization tandem mass spectrometric analysis prevents charging effect. Rapid Commun Mass Spectrom. 2005;19(5):605–10.
24. Liotta LA, Espina V, Wulfkuhle JD, Calvert VS, VanMeter A, Zhou W, et al. Laser-capture microdissection. Nat Protoc. 2006;1(2):586–603.
25. Andersen MK, Høiem TS, Claes BSR, Balluff B, Martin-Lorenzo M, Richardsen E, et al. Spatial differentiation of metabolism in prostate cancer tissue by MALDI-TOF MSI. Cancer Metab. 2021;9(1):9.
26. Goto T, Terada N, Inoue T, Kobayashi T, Nakayama K, Okada Y, et al. Decreased expression of lysophosphatidylcholine (16:0/OH) in high resolution imaging mass spectrometry independently predicts biochemical recurrence after surgical treatment for prostate cancer. Prostate. 2015;75(16):1821–30.
27. Wang X, Han J, Hardie DB, Yang J, Pan J, Borchers CH. Metabolomic profiling of prostate cancer by matrix assisted laser desorption/ionization-Fourier transform ion cyclotron resonance mass spectrometry imaging using matrix coating assisted by an electric field (MCAEF). Biochim Biophys Acta. 2017;1865(7):755–67.
28. Eiersbrock FB, Orthen JM, Soltwisch J. Validation of MALDI-MS imaging data of selected membrane lipids in murine brain with and without laser postionization by quantitative nano-HPLC-MS using laser microdissection. Anal Bioanal Chem. 2020;412(25):6875–86.
29. Stultz J, Fong L. How to turn up the heat on the cold immune microenvironment of metastatic prostate cancer. Prostate Cancer Prostatic Dis. 2021;24(3):697–717.
30. Liu P, Ramachandran S, Ali Seyed M, Scharer CD, Laycock N, Dalton WB, et al. Sex-determining region Y box 4 is a transforming oncogene in human prostate cancer cells. Cancer Res. 2006;66(8):4011–9.
31. Rhodes DR, Yu J, Shanker K, Deshpande N, Varambally R, Ghosh D, et al. Large-scale meta-analysis of cancer microarray data identifies common transcriptional profiles of neoplastic transformation and progression. Proc Natl Acad Sci USA. 2004;101(25):9309–14.
32. Tomlins SA, Mehra R, Rhodes DR, Cao X, Wang L, Dhanasekaran SM, et al. Integrative molecular concept modeling of prostate cancer progression. Nat Genet. 2007;39(1):41–51.
33. Bergholz J, Xiao Z-X. Role of p63 in development, tumorigenesis and cancer progression. Cancer Microenviron. 2012;5(3):311–22.
34. Melino G. p63 is a suppressor of tumorigenesis and metastasis interacting with mutant p53. Cell Death Differ. 2011;18(9):1487–99.
35. Rathod S, Jaiswal D, Bindu R. Diagnostic utility of triple antibody (AMACR, HMWCK and P63) stain in prostate neoplasm. J Family Med Prim Care. 2019;8(8):2651–5.
36. Butler L, Perone Y, Dehairs J, Lupien LE, de Laat V, Talebi A, et al. Lipids and cancer: emerging roles in pathogenesis, diagnosis and therapeutic intervention. Adv Drug Deliv Rev. 2020.
37. Vanauberg D, Schulz C, Lefebvre T. Involvement of the pro-oncogenic enzyme fatty acid synthase in the hallmarks of cancer: a promising target in anti-cancer therapies. Oncogenesis (New York, NY). 2023;12(1):16.
38. Yu Y, Nie Q, Wang Z, Di Y, Chen X, Ren K. Targeting acetyl-CoA carboxylase 1 for cancer therapy. Front Pharmacol. 2023;14:1129010.
39. Han C, Yu G, Mao Y, Song S, Li L, Zhou L, et al. LPCAT1 enhances castration resistant prostate cancer progression via increased mRNA synthesis and PAF production. PLoS ONE. 2020;15(11): e0240801.

40. Sun Q, Fu C, Liu J, Li S, Zheng J. Knockdown of LPCAT1 repressed hepatocellular carcinoma growth and invasion by targeting S100A11. Ann Clin Lab Sci. 2023;53(2):212–21.
41. Moessinger C, Klizaite K, Steinhagen A, Philippou-Massier J, Shevchenko A, Hoch M, et al. Two different pathways of phosphatidylcholine synthesis, the Kennedy Pathway and the Lands Cycle, differentially regulate cellular triacylglycerol storage. BMC cell biology. 2014;15(1):43.
42. Grupp K, Sanader S, Sirma H, Simon R, Koop C, Prien K, et al. High lysophosphatidylcholine acyltransferase 1 expression independently predicts high risk for biochemical recurrence in prostate cancers. Mol Oncol. 2013;7(6):1001–11.
43. Zhou X, Lawrence TJ, He Z, Pound CR, Mao J, Bigler SA. The expression level of lysophosphatidylcholine acyltransferase 1 (LPCAT1) correlates to the progression of prostate cancer. Exp Mol Pathol. 2012;92(1):105–10.
44. Zhao X, Liang J, Chen Z, Jian R, Qian Y, Wang Y, et al. sn-1 Specificity of lysophosphatidylcholine acyltransferase-1 revealed by a mass spectrometry-based assay. Angew Chem (International ed). 2023;62(6):e202215556.
45. Nakanishi H, Shindou H, Hishikawa D, Harayama T, Ogasawara R, Suwabe A, et al. Cloning and characterization of mouse lung-type acyl-CoA:lysophosphatidylcholine acyltransferase 1 (LPCAT1). Expression in alveolar type II cells and possible involvement in surfactant production. J Biol Chem. 2006;281(29):20140–7.
46. Truong JXM, Spotbeen X, White J, Swinnen JV, Butler LM, Snel MF, et al. Removal of optimal cutting temperature (O.C.T.) compound from embedded tissue for MALDI imaging of lipids. Anal Bioanal Chem. 2021;413(10):2695–708.
47. Young RSE, Claes BSR, Bowman AP, Williams ED, Shepherd B, Perren A, et al. Isomer-resolved imaging of prostate cancer tissues reveals specific lipid unsaturation profiles associated with lymphocytes and abnormal prostate epithelia. Front Endocrinol. 2021;12:689600.